

# Phase-resolved modeling of wave interference and its effects on nearshore circulation in a large ebb shoal-beach system

Yu Zhang<sup>1</sup>, Fengyan Shi<sup>2</sup>, James T. Kirby<sup>3</sup>, and Xi Feng<sup>4</sup>

<sup>1</sup>College of Harbor, Coastal and Offshore Engineering, Hohai University

<sup>2</sup>Center for Applied Coastal Research, University of Delaware

<sup>3</sup>University of Delaware

<sup>4</sup>Key Laboratory of Coastal Disaster and Defence (Hohai University), Ministry of Education,

November 24, 2022

## Abstract

A time-domain Boussinesq model was applied to modeling wave interference and its effects on nearshore circulation in San Francisco Bar and the adjacent Ocean Beach, CA. The model predicted the wave interference phenomena caused by the ebb shoal, with interference scales consistent with the Radar observation. Model results reveal that small-scale fingering structures in the wave height distribution result from wave interference and are persistent with nodal lines unchanged with time. Nearshore circulation predicted by the model shows small-scale flow structures tied with the wave modulation patterns. However, the small-scale modulation in the wave field seems not to generate alongshore variation in wave setup at similar scales. Therefore, in a large-scale view, the alongshore currents predicted by the Boussinesq model still keep the general features shown in a wave-averaged model, such as the flow divergence caused by the pressure gradient force associated with the alongshore variation of wave setup. The time-domain Boussinesq model predicted the spatial variability of wave-induced processes. The alongshore-varying wave breakers caused by wave interference are the source of the vorticity generation, inducing energetic vortex eddies nearshore.

# Phase-resolved modeling of wave interference and its effects on nearshore circulation in a large ebb shoal-beach system

Yu Zhang<sup>1,2</sup>, Fengyan Shi<sup>1</sup>, James T. Kirby<sup>1</sup>, Xi Feng<sup>2</sup>

<sup>1</sup>Center for Applied Coastal Research, Department of Civil and Environmental Engineering, University of Delaware,  
Newark, DE 19716 USA

<sup>2</sup>College of Harbor, Coastal and Offshore Engineering, Hohai University, Nanjing, China

## Key Points:

- A time-domain Boussinesq model reproduced wave interference observed at Ocean Beach, CA.
- The model reveals small-scale persistent fingering structures in the wave height distribution tied with nearshore flow structures not predicted in the traditional nearshore circulation model.
- Alongshore-varying wave breakers caused by wave interference are the source of vorticity generation, inducing energetic vortex eddies nearshore.

**Abstract**

A time-domain Boussinesq model was applied to modeling wave interference and its effects on nearshore circulation in San Francisco Bar and the adjacent Ocean Beach, CA. The model predicted the wave interference phenomena caused by the ebb shoal, with interference scales consistent with the Radar observation. Model results reveal that small-scale fingering structures in the wave height distribution result from wave interference and are persistent with nodal lines unchanged with time. Nearshore circulation predicted by the model shows small-scale flow structures tied with the wave modulation patterns. However, the small-scale modulation in the wave field seems not to generate alongshore variation in wave setup at similar scales. Therefore, in a large-scale view, the alongshore currents predicted by the Boussinesq model still keep the general features shown in a wave-averaged model, such as the flow divergence caused by the pressure gradient force associated with the alongshore variation of wave setup. The time-domain Boussinesq model predicted the spatial variability of wave-induced processes. The alongshore-varying wave breakers caused by wave interference are the source of the vorticity generation, inducing energetic vortex eddies nearshore.

**Plain Language Summary**

Coherent wave interference is a common phenomenon caused by surface wave interaction with seabed topography, nearshore structures, or coastal currents. It cannot be predicted by the conventional wave-averaged model based on the Radiative Transfer Equation. The objective of the study is to use a time-domain Boussinesq model to predict the wave interference at the ebb-tidal delta of San Francisco, CA, which was observed by Radar measurements. The model shows small-scale fingering structures in the wave height distribution resulting from wave interference with alongshore scales consistent with the measurements. The small-scale variation in the wave field is persistent, inducing small-scale flow structures nearshore. However, the wave field modulation seems not to generate alongshore variation in wave setup in the small scales. Therefore, in a large-scale view, the alongshore currents predicted by the Boussinesq model still keep the similar features as shown in a wave-averaged model, such as the flow divergence caused by the pressure gradient force associated with the alongshore variation of wave setup. The time-domain Boussinesq model also shows energetic vortex eddies in the surf zone, which are generated by alongshore varying wave breakers tied with wave interference.

**1 Introduction**

Coherent wave interference commonly occurs in the coastal ocean due to surface wave interaction with the inner-shelf topography, coastal structures, or coastal currents [Smit and Janssen, 2013]. It is more significant for narrow-band waves, i.g., swells, which exhibit persistent wave height variability in the laboratory [Vincent and Briggs, 1989; Chawla et al., 1998] and field [Smit et al., 2016]. Breaking waves under such coherent interference influences can generate nearshore circulation cells, which are more stationary [Dalrymple, 1975; Dalrymple et al., 2011] in contrast to transient circulation cells induced by non-coherent short-crested waves [Johnson, 2004; Spydell and Feddersen, 2009].

Modeling of coherent wave interference and associated wave-induced processes is challenging, especially at field scale. Traditional field-scale wave prediction models, such as SWAN [Booij et al., 1999] or WaveWatch [Tolman, 1991], are stochastic models based on the Radiative Transfer Equation (RTE), which requires the assumptions for a slowly varying medium and statistically independent wave components [Komen et al., 1996]. Such assumptions make the model unable to resolve inhomogeneous wave patterns caused by coherent wave interference. These limitations have been partially alleviated by the recent work of Smit and Janssen [2013], who introduced the second-order statistics into a stochastic wave model, allowing the modeling of statistical wave interference caused by wave refraction and diffraction in coastal seas. The model was validated against in situ data measured during the NCEX

20 experiment in the Scripps and La Jolla Canyon [*Smit et al.*, 2015], which showed that the  
21 model based on the quasi-coherent statistical theory is able to predict statistical interference  
22 and associated inhomogeneities in the wave field. More recently, *Akrish et al.* [2020] have  
23 extended the quasi-coherent model to include the effect of wave-current interaction.

24 A more direct way to model wave interference is to use phase-resolving wave models,  
25 such as Boussinesq models [e.g., *Shi et al.*, 2012] or non-hydrostatic models [e.g., *Ma et al.*,  
26 2012]. Because wave phase information is explicitly retained, the wave interference caused  
27 by wave coherence can be directly modeled. Another advantage in using such a phase-resolving  
28 wave model is that the model predicts not only wave interference patterns but also wave-wave  
29 interaction and breaking-induced nearshore circulation. However, due to the high computa-  
30 tional cost of a phase-resolving model, large-domain field applications of such models have  
31 rarely been carried out.

32 Among the available classes of phase-resolving wave model, Boussinesq-type wave  
33 models are less time-consuming than non-hydrostatic wave models using a Pressure Poisson  
34 solver [for example, NHWAVE or SWASH *Ma et al.*, 2012; *Zijlema et al.*, 2011]. The paral-  
35 lel computing and the adaptive mesh refinement (AMR) techniques make the model readily  
36 feasible to be used for simulations of surface wind waves over domains with dimensions of  
37 tens of kilometers [e.g., *Chakrabarti et al.*, 2017].

38 The objective of this study is to investigate wave interference patterns arising in prop-  
39 agation of nearly unidirectional waves over bathymetry control and small-scale variability in  
40 shoreline circulation patterns using a phase resolving model approach. The study site is the  
41 San Francisco Bar and the adjacent Ocean Beach as shown in Figure 1.

42 Figure 1 shows the San Francisco Bar and the adjacent Ocean Beach. *Smit et al.* [2016]  
43 reported X-band radar observations which showed strong wave interference patterns in the  
44 nearshore region [see Figure 3 in *Smit et al.*, 2016]. Their analysis using the coupled-mode  
45 spectrum revealed that, during energetic swell events, the nearshore wave field is comprised  
46 of two coherent wave trains originating from the same offshore wave source. Due to wave  
47 refraction over the San Francisco Bar, the offshore waves are directionally separated into two  
48 swell systems behind the bar, resulting in a coherent interference pattern landward of the  
49 bar region. Figure 1 (b) illustrates the wave interference pattern seen in Google Earth im-  
50 agery taken on March 14th, 2000. The wave height measured at the offshore CDIP buoy 029  
51 (<http://cdip.ucsd.edu>), located at  $37^{\circ}56'45''\text{N}, 23^{\circ}28'12''\text{W}$ , varied from 1.45 – 2.14 m on that  
52 day, with peak wave periods of 9.8 - 16.7 s. The averaged incident angle was  $288^{\circ}$ .

53 The influence of the San Francisco Bar on nearshore hydrodynamics and sediment  
54 transport has been investigated by many researchers. The San Francisco Bar is a large-scale  
55 horseshoe-shaped ebb-tidal delta as shown in Figure 1 (a). Earlier studies have shown the  
56 effect of wave focusing by the southern shoal, resulting in alongshore variations of wave  
57 energy and wave set-up along the adjacent Ocean Beach [*Eshleman et al.*, 2007; *Shi et al.*,  
58 2011; *Barnard et al.*, 2012; *Hansen et al.*, 2014]. The alongshore pressure gradient caused  
59 by wave set-up variation is the dominant force in the alongshore momentum balance, driv-  
60 ing nearshore circulation and sediment transport on the beach [*Shi et al.*, 2011; *Hansen et al.*,  
61 2013, 2014].

62 Numerical models used in previous studies of this region have been based on cou-  
63 pled wave and circulation models, such as the Nearshore Community Model [NearCoM, *Shi*  
64 *et al.*, 2005; *Chen et al.*, 2014] and Delft3D [*Lesser et al.*, 2004]. The wave component in  
65 both models mentioned above is the wave model SWAN [*Booij et al.*, 1999]. Wave interfer-  
66 ence and its effect on nearshore circulation could not be modeled due to the phase-averaging  
67 nature of the model theory. Our questions are 1) how does the wave interference affect the  
68 wavefield in the nearshore region of Ocean Beach; 2) how does the wave interference affect  
69 wave-induced circulation; 3) what is the difference in model prediction between a phase-  
70 averaging model and phase-resolving model.

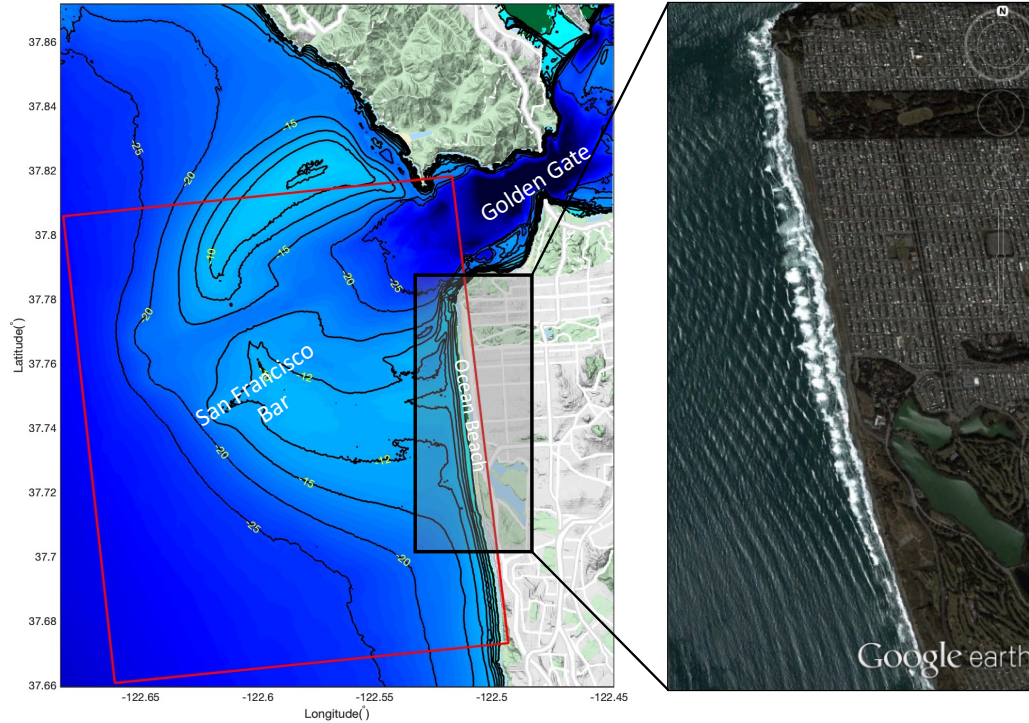


**Figure 1.** (Left) the ebb tidal delta (San Francisco Bar) and Ocean Beach. The computational domain is denoted by the red block. Solid black lines are depth contours. (Right) interference patterns of swells at Ocean Beach observed in the Google Earth imagery taken on March 14th, 2000 (map ©2021 Google, ©TerraMetrics).

71 To address these questions, we carried out a numerical study using the time-domain  
 72 Boussinesq wave model, FUNWAVE-TVD, in a large-scale domain (10's km) to cover the  
 73 entire wave propagation and evolution process, including wave shoaling, refraction, inter-  
 74 ference, breaking, and wave-induced nearshore circulation. The numerical results were com-  
 75 pared with results from the coupled wave and circulation model, NearCoM, which cannot  
 76 predict wave interference and its nearshore effects.

77 In the rest of the paper, section 2 briefly reviews the study site and hydrodynamic con-  
 78 ditions, emphasizing the wave interference phenomenon caused by the southern shoal. In  
 79 section 3, the numerical model and model setup are described. The basic characteristics of  
 80 wave interference are presented using a monochromatic wave simulation and wave ray racing  
 81 analysis in section 4. Section 5 provides results of the wave field predicted by the Boussinesq  
 82 model with comparisons with the measured data and model results from the phase-averaged  
 83 model, SWAN. In section 6, wave-averaged processes are discussed according to the compar-  
 84 isons between the Boussinesq model and the phase-averaged circulation model. Findings are  
 85 summarized in section 7.

## 86 2 Wave interference caused by San Francisco Bar

87 San Francisco Bar is a large-scale ebb-tidal shoal offshore of the Golden Gate of the  
 88 San Francisco Bay as shown in Figure 1. The minimum depths are about 9.5 m and 10.5  
 89 m on the northern and southern lobes, respectively. Shoreward of the south lobe is Ocean  
 90 Beach, a 7-km long sandy beach located along the western, ocean-facing boundary of the  
 91 city of San Francisco. The wave climate of Ocean Beach is characterized by large-scale wave

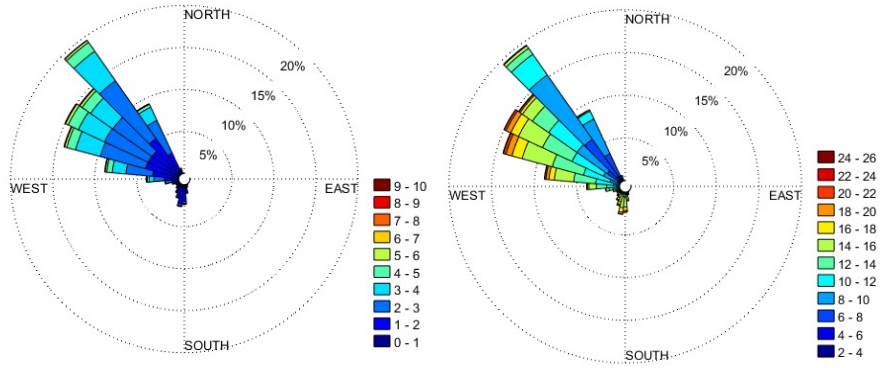


**Figure 2.** Wave statistics using the measured data from 1996-2021 at CDIP buoy 029 buoy. (Left) wave height (m) and dominant wave angle. (Right) wave peak period (s) and dominant wave angle.

height variability along the beach due to wave refraction over the shoal (Shi et al., 2011, Hansen et al., 2014). Nearshore circulation at this larger scale is governed by the alongshore pressure gradient generated by the variation in wave setup. It is also affected by the tide-induced alongshore pressure gradient due to the presence of the Golden Gate inlet (Hansen et al., 2013). Because Ocean Beach is directly exposed to energetic ocean swells, strong wave interference patterns occur at Ocean Beach, as reported by Smit et al. (2016). The wave interference causes persistent wave height variability at the Ocean Beach, the effect of which on nearshore circulation is unknown.

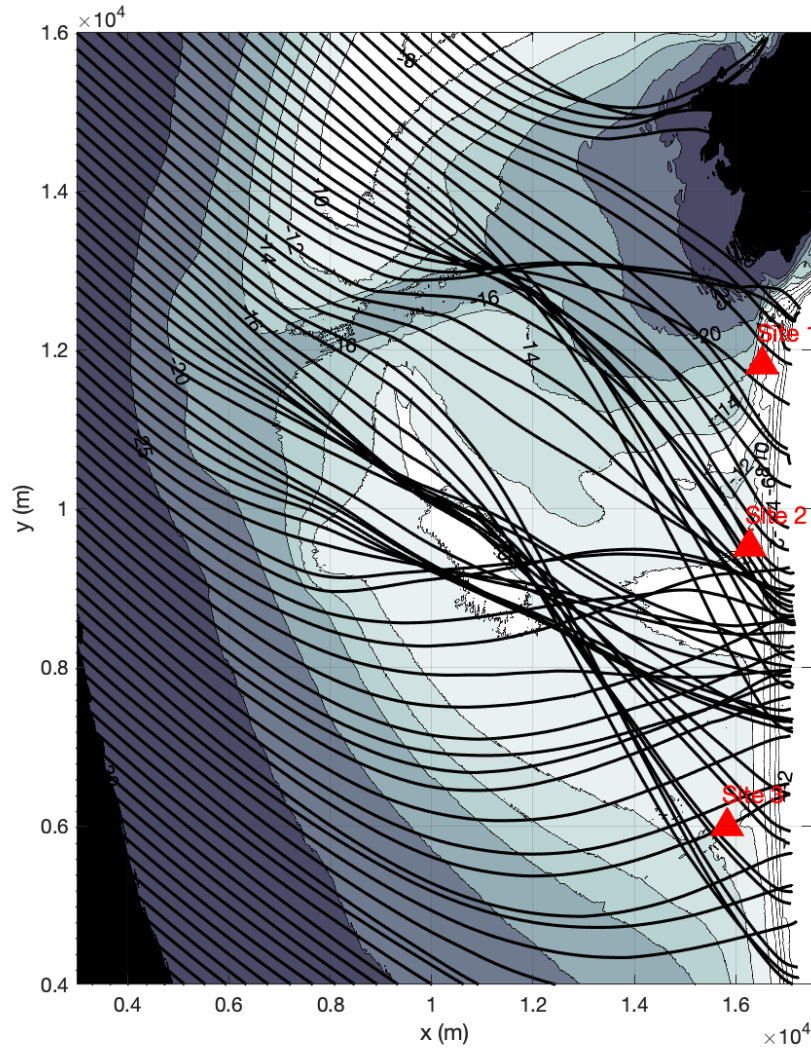
Ocean swell with periods ranging from 11.4s - 26.6s [O'Reilly et al., 2016] in this region is typically generated by large winter Pacific Ocean storms, which arrive from northwest to west. Lower-energy south swell events can occur during the summer, with a lower probability than the winter swell. Figure 2 shows plots of wave height (left) and dominant wave angle (right) analyzed using data measured during 1996 – 2021 at CDIP buoy 029 (<http://cdip.ucsd.edu>), located at  $37^{\circ}56'45''\text{N}$ ,  $23^{\circ}28'12''\text{W}$ . According to the data, more than 42% of wave events are swell waves, and about 70% of swell come from NWW with the averaging direction of  $295^{\circ}$  and an average period of 14.4 s.

Figure 3 shows the wave ray tracing for offshore swell with a direction of  $300^{\circ}$  and a period of 15 s propagating over the San Francisco Bar and onto Ocean Beach. To facilitate the model setup described in the next section, we rotated the coordinates by  $7^{\circ}$  counter-clockwise to make the shoreline align with the  $y$ -direction in the local Cartesian coordinates  $(x, y)$ . As shown in the figure, wave refraction over the shoal causes strong wave interference with significant wave-ray crossing at the nearshore region.

During the summer of 2005 and the winter of 2006, two field experiments were performed to examine spatial differences in wave and current patterns offshore of Ocean Beach (Barnard et al., 2007, Shi et al., 2011). Site 1 – Site 3 are three measurement sites aligned approximately alongshore in water depths from 7 to 13 meters. Detailed deployment locations and durations are referred to Shi et al. (2011).

### 3 Time-domain Boussinesq wave model

FUNWAVE is a widely-accepted public domain Boussinesq-type wave model in the nearshore and tsunami research community. The original generation of the code was developed by Kennedy et al. [2000] and Chen et al. [2000], based on the fully nonlinear Boussinesq equations of Wei et al. [1995]. Subsequent improvements in the formulation covering



**Figure 3.** Wave ray tracing for offshore waves with an incident angle of  $\theta = 300^\circ$  and a period of  $T = 15$  s. Measurement locations, Site 1 - Site 3 are denoted by red triangles. The wave ray crossing appears south of the nearshore measurement location, Site 2.

124 improvements in nonlinear mode-coupling [Kennedy *et al.*, 2001] and treatment of the vertical  
 125 component of vorticity [Chen *et al.*, 2003; Chen, 2006] have been incorporated in the  
 126 recent development of a Total Variation Diminishing (TVD) version, FUNWAVE-TVD,  
 127 motivated by recent needs for modeling surfzone dynamics, tsunami waves, and coastal in-  
 128 undation processes in both global and coastal scales [Shi *et al.*, 2012]. The model has been  
 129 parallelized using the Message Passing Interface (MPI) and optimised for use on large-scale,  
 130 high-performance computing system [Lam *et al.*, 2018]. Further extensions incorporating  
 131 GPU-acceleration techniques [Yuan *et al.*, 2020] will further increase the feasibility of the  
 132 model's use for large-domain and long-time simulations. For irregular wave applications,  
 133 the model is equipped with an internal wavemaker that can generate monochromatic or di-  
 134 rectional spectral waves based on bulk parameters or measured spectral data. Recently, the

wavemaker has been revised to address the problem of spurious spatial correlations occurring in irregular waves, resulting from discretization of target spectra over a uniform grid of frequencies and alongshore wavenumbers [Salatin *et al.*, 2021].

According to the model applicability related to the weakly dispersion assumption,  $kh \leq 3$  [Kirby, 2016], we confine the computational domain nearshore up to the water depth of 35 m, covering the southern ebb-tidal shoal and Ocean Beach, as shown in Figure 1 (red block). The computational grid was constructed using the 10-m digital elevation model (DEM) [Fregoso *et al.*, 2017], which combines bathymetry and topography data with the vertical datum of NAVD88. The mean tide level (MTL) was converted based on the datum at NOAA station 9414290 in San Francisco, CA. The grid has  $8712 \times 7960$  grid points with grid sizes of  $2 \times 2$  m, covering a region of 17.424 km and 15.920 km in the  $x$ - and  $y$ -directions, respectively.

We applied the internal wavemaker, which can generate monochromatic and spectral waves for given directional spectra (e.g., TMA, JONSWAP spectra, or measured spectral data). The wavemaker is located at a 35-m flat bottom (truncated near 35 m contour), 800 m away from the west boundary. A 500m-wide sponge layer was specified at the western boundary to absorb waves propagating seaward from the internal generation region. To apply the lateral periodic boundary condition, we modified the bathymetry and topography at the inlet region to make the grid cyclic in the south-north direction with a 4-km wide buffer region on the north side. Such a reconstruction of the grid does not affect modeled wave field nearshore of Ocean Beach because wave directions considered in this study are basically from NWW. A constant bottom drag coefficient of  $C_d = 0.002$  in the quadratic friction formula was applied in all cases below.

#### 4 Basic characteristics of wave interference in a monochromatic wave field

To demonstrate the basic characteristics of coherent wave interference caused by the tidal ebb shoal, we carried out a simulation of monochromatic waves with an incident angle of  $\theta = 300^\circ$ , a period of  $T = 15s$ , and wave height of  $H = 2m$ , which are typical bulk parameters for winter swells. Figure 4 provides a snapshot of wave surface elevation with wave ray tracing (thick lines) superimposed on the wave surface. Due to the modification for the periodic boundary condition mentioned above, the bathymetric contours in the figure are slightly different from that shown Figure 3 in the northern region. For this reason, the wave rays in the north of the domain are not shown. The figure shows that, before reaching the shoal, waves are regular plane waves with approximately uniform wave height and direction. Wave shoaling effects are significant as waves climb over the shoal, as indicated by large peaks (sharp red color) and lower troughs (blue color) on the shoal. Wave refraction on the shoal causes convergence and divergence of wave rays, inducing larger wave heights in the focusing zone and lower wave heights in the shadow zones (both southern and northern sides of the focusing zone). Wave diffraction patterns are also shown in the shadow zone. Further nearshore, standing wave patterns caused by the wave interference appear in the wave-ray crossing region, which covers a similar area as the wave focusing zone. Waves break near the shoreline, inducing large wave setup as indicated by the warmer color in the surf zone, consistent with the wave setup patterns modeled by Shi *et al.* [2011].

Figure 5 shows the same snapshot as Figure 4, but are 1-D plots along two wave rays denoted by the red lines, Ray 1 and Ray 2, respectively, in Fig. 4. Ray 1 traces waves across the top of the shoal, while Ray 2 is located south of Ray 1, passing the shadow zone. Along Ray 1, wave shoaling occurs as waves enter the shallow shoal (see bathymetric profile (b),  $x < 10,000m$ ). As waves continue propagating shoreward, a large variation in wave amplitude appears though the water depth shoreward is relatively flat (see b). The large variation in amplitude results from the standing wave patterns as revealed in Figure 4. In contrast to Ray 1, waves propagating along Ray 2 do not show shoaling-induced wave height increase because waves along Ray 2 are inside the shadow zone and the seabed slope is milder com-

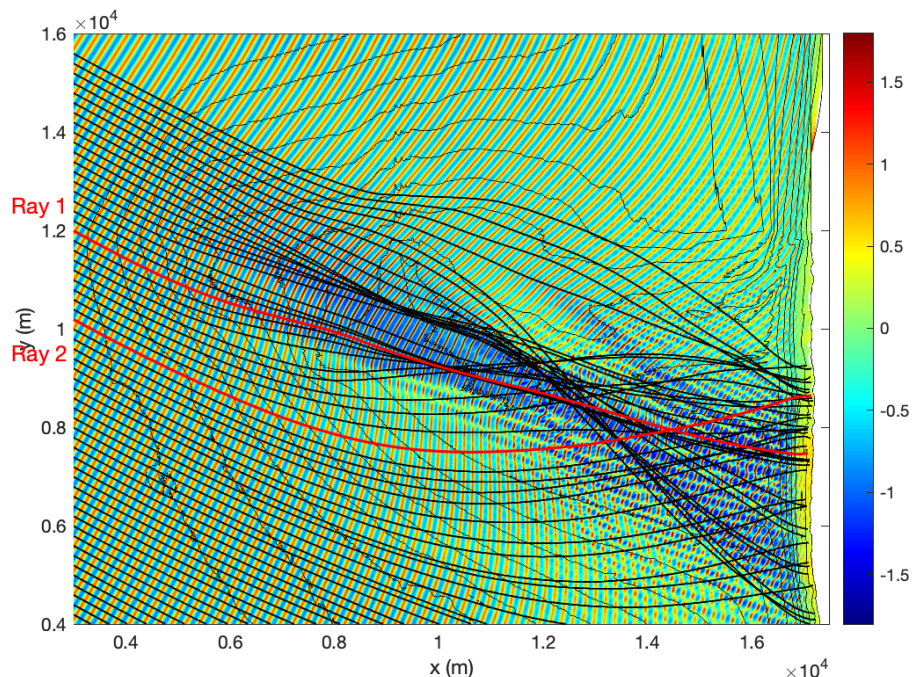


**Figure 4.** A snapshot of wave surface elevation (color) modeled for offshore monochromatic waves with an incident angle of  $\theta = 300^\circ$ , a period of  $T = 15s$ . Thin solid lines are bathymetric contours, thick solid lines denote wave rays. The red solid lines represent two wave rays selected for 1D surface elevation plots in Fig. 5.

186 pared to the profile along Ray 1. However, large waves emerge nearshore ( $x > 12,000m$ ) as  
 187 the wave ray bends northwards, entering the wave interference region.

188 The alongshore modulation scales can be represented by sizes of standing wave cells  
 189 at a certain water depth. They can be calculated by the wave length and the wave cross-  
 190 ing angles obtained from wave ray directions. Figure 6 shows alongshore sizes of standing  
 191 wave cells at 10 m water depth offshore of Ocean Beach calculated based on wave tracing for  
 192 waves of  $T_p = 15$  s with different incident angles. It appears that the sizes of standing wave  
 193 cells do not vary much with the incident wave angles, except for the incident angle of  $165^\circ$ ,  
 194 in which wave interference occurs at the northern part of Ocean Beach. The sizes are in 150  
 195 ~ 310 m, which is generally consistent with the alongshore sizes of 100 ~ 300 m observed in  
 196 *Smit et al.* [2016]. The size may change with the incident wave period and water depth.

## 197 5 Spectral wave field

198 Based on the availability of field data, we selected two wave conditions that occurred  
 199 during the observation periods in summer 2005 and winter 2006, respectively, both of which  
 200 favor the generation of wave interference patterns in terms of wave incident angle. Case 1  
 201 simulates the wave condition appeared on July 12, 2005 with the significant wave height  
 202  $H_{sig} = 2.49$  m, the peak period,  $T_p = 11.1$  s, and dominant wave angle  $\theta_p = 290^\circ$  measured  
 203 at the CDIP 029 buoy. Case 2 is a major storm event occurred on January 4, 2006 with  $H_{sig}$   
 204  $= 5.1$  m,  $T_p = 14.29$  s, and  $\theta_p = 297^\circ$ . The wave input conditions for the Boussinesq model  
 205 are based on wave bulk parameters resulting from the large-domain model, NearCoM [*Shi*  
 206 *et al.*, 2011]. The JONSWAP spectrum with  $\gamma = 3.3$  and the directional spreading parame-  
 207 ter  $\sigma_\theta = 10^\circ$  was partitioned into 1125 wave components, which are randomly phased with

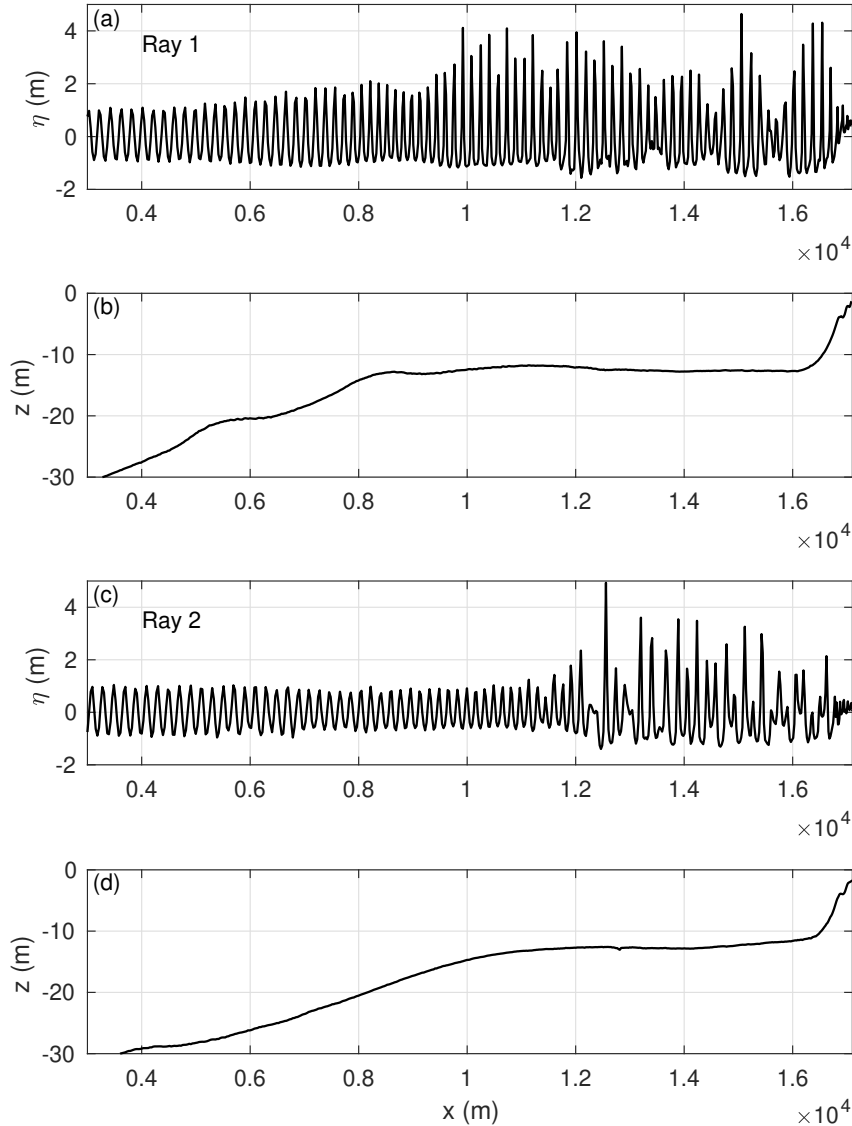


**Figure 5.** Snapshots of wave surface elevation (a, c) and bathymetric profiles (b, d) along the two wave rays selected in Figure 4.

208 zero-coherence [Salatin *et al.*, 2021]. The water depth is adjusted based on the tidal level  
 209 recorded at the NOAA station 9414290.

## 210 5.1 FUNWAVE results

211 Figure 7 shows a snapshot of surface elevation after a spin-up period of 1800 s. The  
 212 figure shows wave shoaling at the ebb-shoal, focusing due to wave refraction, and remarkable  
 213 standing wave features caused by wave interference, generally consistent with the regular  
 214 wave case. The wave interference concentrates at the nearshore region south of Site 2, simi-  
 215 lar to the regular wave case due to the similar offshore incident angle.

216 Significant wave height was estimated using the zero-crossing method for the time pe-  
 217 riod of 1800 – 3000 s in the simulation. As shown in Figure 8, large wave heights occur at  
 218 the ebb-shoal region and the nearshore area behind the shoal due to wave focusing. In partic-

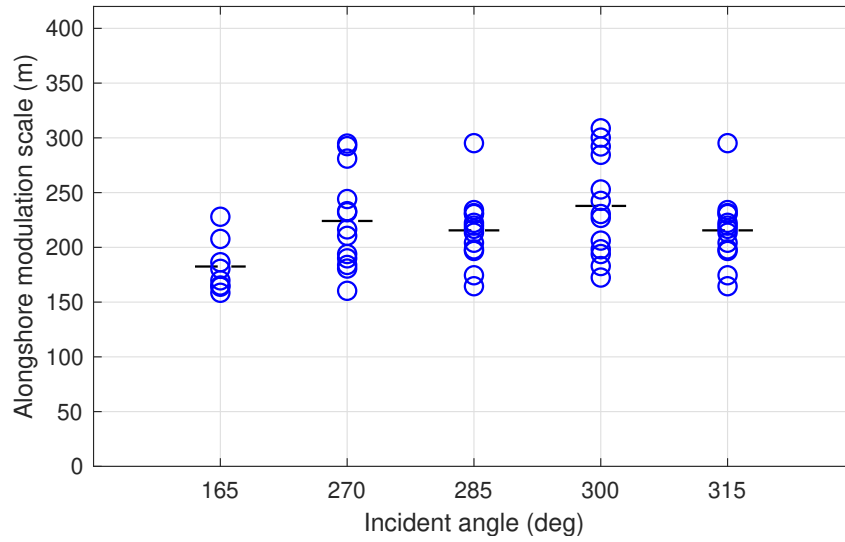


**Figure 6.** Alongshore sizes of standing wave cells at 10 m water depth calculated from wave tracing for offshore waves with different incident angles (Nautical Convention) and  $T_p = 15$  s. Short black lines represent the values averaged over interference rays passing 10 m water depth contour.

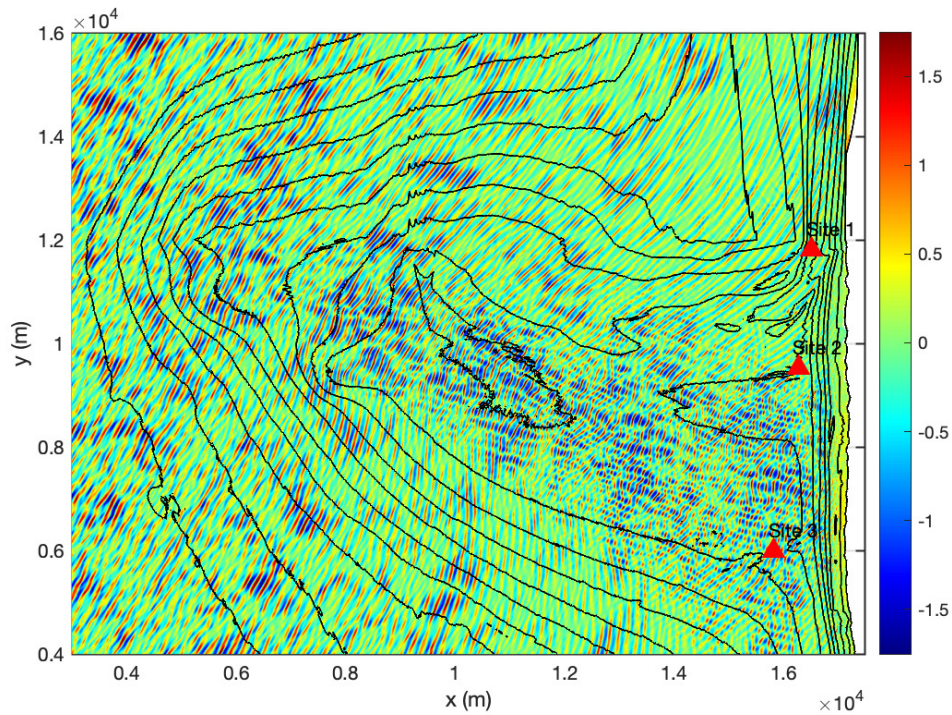


**Figure 7.** A snapshot of wave surface elevation (color) for Case 1 simulated by Boussinesq model. The wave condition occurred on July 12, 2005 with  $H_{sig} = 2.49$  m,  $T_p = 11.1$  s, and  $\theta_p = 290^\circ$  measured at the CDIP 029 buoy. Red triangles represent measurement locations, Site 1 - 3 [Shi *et al.*, 2011; Hansen *et al.*, 2013].

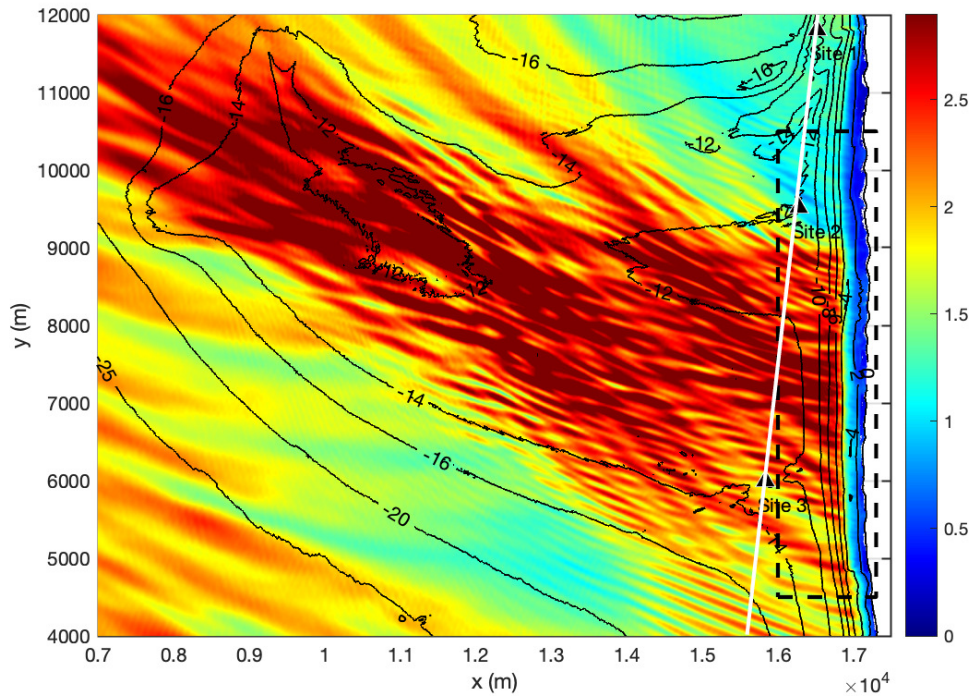


**Figure 8.** Distribution of the significant wave height estimated using zero-crossing in a time interval of 1200 s (1800 s - 3000 s). Case 1:  $H_{sig} = 2.49$  m,  $T_p = 11.1$  s, and  $\theta_p = 290^\circ$  measured at the CDIP 029 buoy. Black triangles represent measurement locations, Sites 1 - 3. The rectangle bounded by black dashed lines is the region shown in Figure 12. The white line is the transect crossing the measurement locations, Site 1 – Site 3.

219 ular, wave height in the nearshore region exhibits fingering patterns arising from the oblique  
 220 intersection of component waves, as in the monochromatic case, with magnitudes fluctuating  
 221 in the alongshore direction.

222 Figure 9 compares the modeled wave height with data along the wave measurement  
 223 transect denoted by the white line in Figure 9. To examine the persistence of the wave height  
 224 distribution, we calculated the wave height in the different averaging periods, 300 s, 600 s,  
 225 and 1200 s, respectively, in the comparison. It is shown that, despite the different averaging  
 226 periods used for wave height estimate, the recurring modulation patterns are similar with  
 227 nodal locations approximately fixed, suggesting a pronounced persistent feature associated  
 228 with wave interference. The magnitudes of fluctuation (from node to antinode) are around 1  
 229 m, with the maximum magnitude appearing at the center of the focusing region. Because the  
 230 data at Site 1 is unavailable, the modeled wave heights are compared with the data at Site 2  
 231 and Site 3, respectively, with good agreement. The comparison also shows that the measure-  
 232 ments are too sparse in space to capture the wave height fluctuation patterns.

233 Case 2 is a major storm condition with  $H_{sig} = 5.1$  m,  $T_p = 14.29$  s, and  $\theta_p = 297^\circ$   
 234 observed at CDIP 029 buoy. Because the wave incident angle is close to Case 1, the wave  
 235 propagation and evolution patterns are similar to Case 1 and are thus not shown here. Fig-  
 236 ure 10 shows the same plot as Fig. 9 but for Case 2 (Note: the data is unavailable at Sites 1  
 237 and 2). Again, the fluctuation patterns in the alongshore wave height distribution are quite  
 238 persistent, reflected by the fixed nodal locations obtained from different averaging periods.

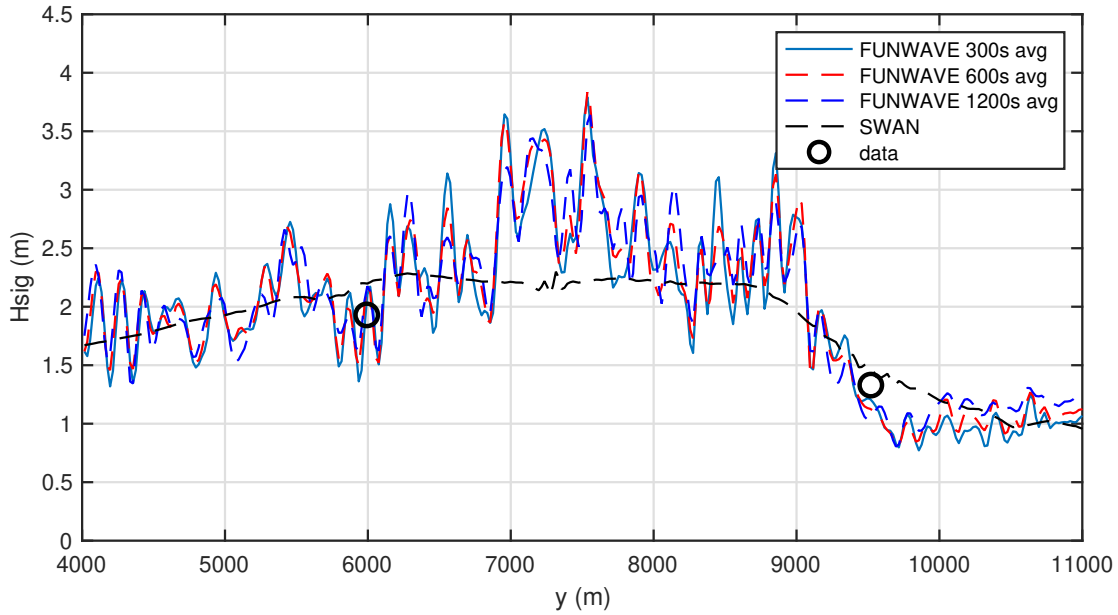


**Figure 9.** Alongshore wave height distributions estimated for averaging periods with durations of 300 s, 600 s, and 1200 along the wave measurement transect, Site 1 - Site 3. Case 1:  $H_{sig} = 2.49$  m,  $T_p = 11.1$  s, and  $\theta_p = 290^\circ$  measured at the CDIP 029 buoy. The dashed line represents the result from the SWAN model, discussed in section 5.2.

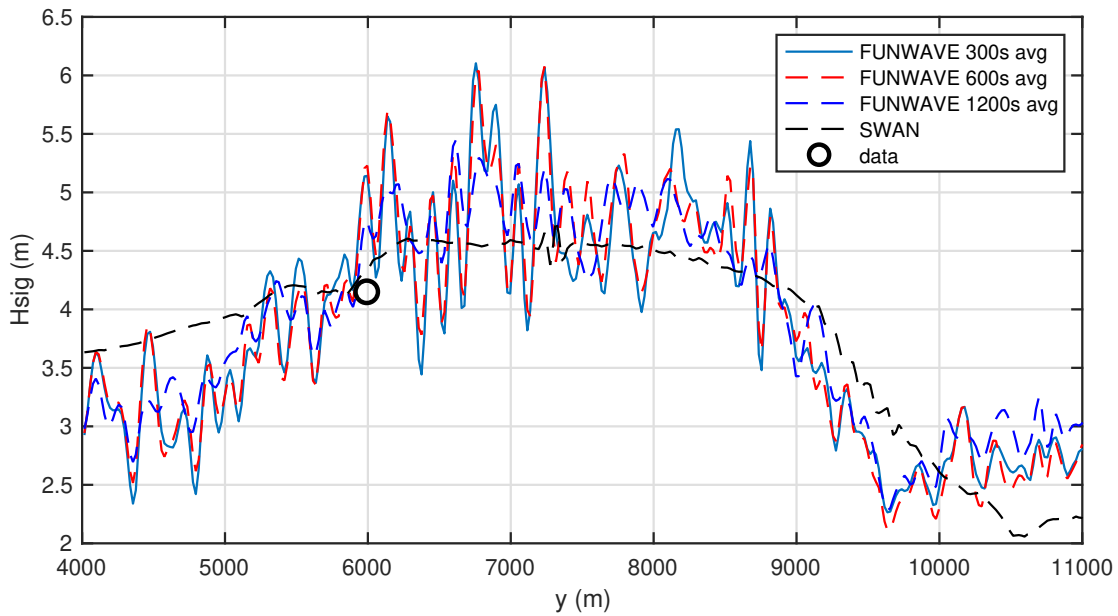


**Figure 10.** The same plot as Fig. 9, but for Case 2.  $H_{sig} = 5.1$  m,  $T_p = 14.29$  s, and  $\theta_p = 297^\circ$  measured at the CDIP 029 buoy.

239  
240

The magnitudes of the wave height modulation reach to 2 m, much larger than that in Case 1, expecting a stronger effect on nearshore circulation.

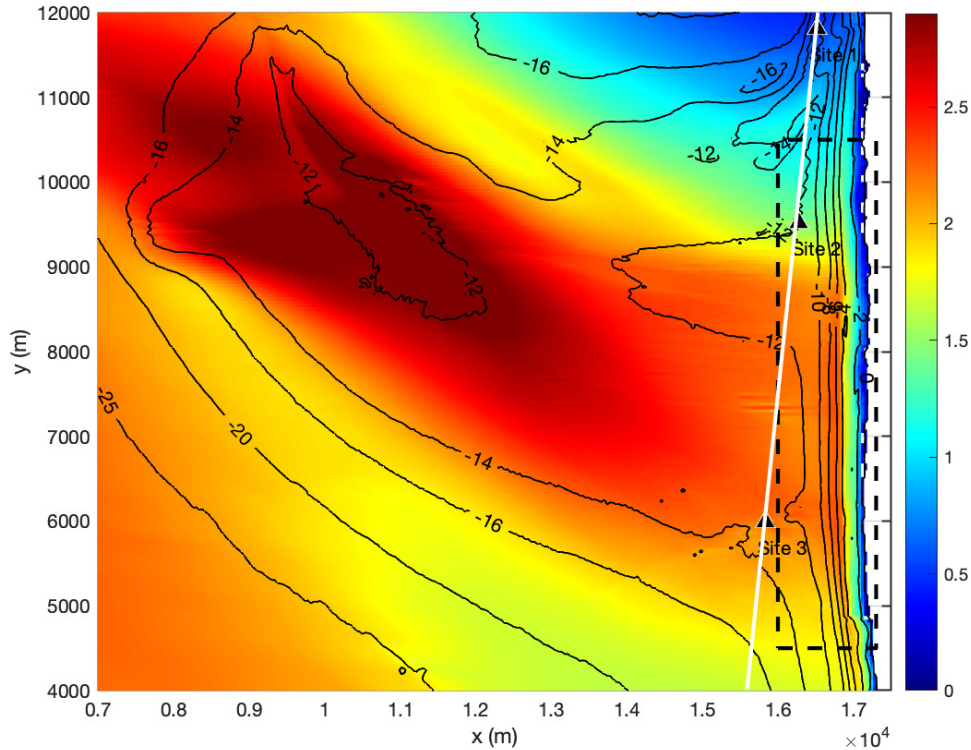


**Figure 11.** Wave height distribution from the SWAN model. Case 1:  $H_{sig} = 2.49$  m,  $T_p = 11.1$  s, and  $\theta_p = 290^\circ$  measured at the CDIP 029 buoy. The rectangle bounded by black dashed lines rectangle is the region shown in Figure 14. The white line is the transect crossing the measurement locations, Site 1 – Site 3.

241

## 5.2 Comparison to the SWAN model

242

243

244

245

246

247

248

249

It is interesting to compare the phase-resolving Boussinesq model and the conventional phase-averaged wave model that cannot model wave interference. The wave model in the previous studies of San Francisco Bar is the SWAN model, such as in NearCoM [Shi *et al.*, 2011] and Delft-3D [Hansen *et al.*, 2013]. Here, we applied the NearCoM model with the same bathymetric data (modified periodic bathymetry) and the same wave conditions as FUNWAVE. To make the model comparable to FUNWAVE, we only considered the surface wave boundary condition, ignoring tidal current, wind, and other external forcing used in Shi *et al.* [2011]. A uniform rectangular grid was used with a grid resolution of 20 m.

250

251

252

253

254

255

256

257

258

259

Figure 11 shows the wave height distribution from the SWAN model. Wave focusing causes large wave heights mainly distributed on the shoal. Compared to the FUNWAVE results shown in Figure 8, the major difference between the two models can be found in the nearshore region, where FUNWAVE predicts the fingering patterns of the wave field, while SWAN provides a smooth distribution of wave height. A striking difference can be seen in the 1D plot of wave height comparisons along the measurement transect shown in Figures 9 and 10. The SWAN model does not predict the large magnitude fluctuations as in the FUNWAVE model. In addition, FUNWAVE predicts generally larger wave heights at the center of the focusing region than SWAN, probably due to different wave dissipation mechanisms in FUNWAVE, similar to the finding in Geiman *et al.* [2011] who also compared FUNWAVE

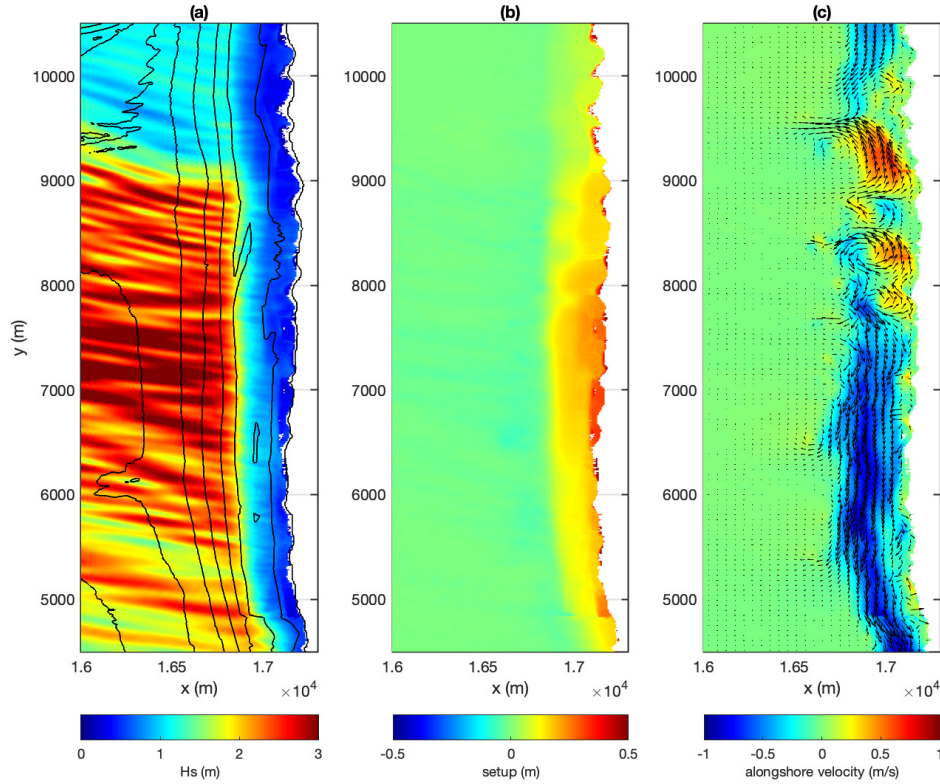


**Figure 12.** Wave height distribution (a), wave setup (b), and wave-induced circulation (c, color represents alongshore velocity) in the nearshore region denoted in the dashed line block in Figure 8. The wave-averaged quantities are analyzed over the time period of 1200 s. Case 1:  $H_{sig} = 2.49$  m,  $T_p = 11.1$  s, and  $\theta_p = 290^\circ$  measured at the CDIP 029 buoy.

260 and SWAN in the simulation of the Rip Current Experiment [RCEX, *Brown et al.*, 2009;  
 261 *MacMahan et al.*, 2010].

## 262 6 Wave-averaged processes

263 The previous studies showed that the nearshore circulation at Ocean Beach exhibits re-  
 264 markable two-dimensional features. Although Ocean Beach has a nearly alongshore uniform  
 265 bathymetry, the nearshore wave field is strongly alongshore varying because wave refraction  
 266 over the ebb shoal causes wave focusing toward a narrow region at Ocean Beach. Due to the  
 267 spatial variation in wave breaker height, wave-induced setup appears to have a strong along-  
 268 shore nonuniformity, resulting in a dramatic change in the pressure field [*Shi et al.*, 2011;  
 269 *Hansen et al.*, 2014]. The pressure gradient can be a dominant force driving nearshore cir-  
 270 culation in the surf zone of Ocean Beach. For the time-domain Boussinesq model, wave-  
 271 averaged quantities, such as wave setup, alongshore current and rip current velocities are  
 272 usually obtained by wave averaging over a number of wave periods [*Chen et al.*, 2003].

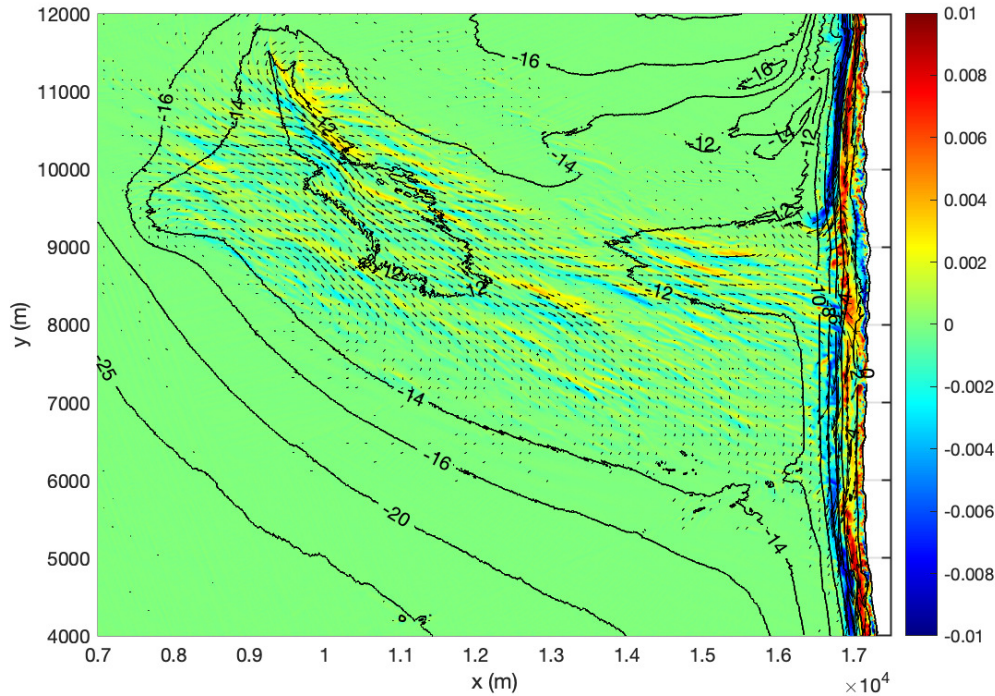


**Figure 13.** Current (arrows) and vorticity field (color) for Case 2. The wave-averaged quantities are analyzed in the time period of 1200 s. Wave conditions:  $H_{sig} = 5.1$  m,  $T_p = 14.29$  s, and  $\theta_p = 297^\circ$  measured at the CDIP 029 buoy.

273

## 6.1 FUNWAVE results

274

275

276

277

278

279

280

281

282

283

284

285

286

287

288

289

290

Figure 12 shows wave-averaged results from Case 1, including the significant wave height (a), wave setup (b), and nearshore circulation in the nearshore region denoted in the dashed line block in Figure 8. The wave-averaged quantities were calculated in a 1200 s-long time period starting from the simulation time of 1800 s to 3000 s. As shown in (a), large wave heights are basically confined in the 5000 m-long offshore region,  $y = 5000 \sim 9000$  m, with the maximum value around the center of the region. Wave height modulations caused by wave interference are in small-scale, in sizes of  $200 \sim 300$  m. Waves break in shallow water and induce wave setup in the surfzone (b). Due to the alongshore variation in offshore wave height, wave setup appears to be alongshore varying. It is interesting that the wave setup does not respond closely to the small-scale feature of the offshore wave height modulation and turns to be smoothly distributed alongshore. Figure 12 (c) shows the wave-induced nearshore circulation with arrows representing current velocity vectors and color for alongshore component velocity (blue for southward). As waves come from northwest, alongshore currents are generally southward. However, the alongshore pressure gradient associated with alongshore nonuniform wave setup induces the northward forcing, causing flow reversal, or divergence, as shown in the north region ( $8000 \sim 9500$  m). The pressure-gradient-driven process described here is consistent with the finding of *Shi et al.* [2011].

291

292

293

294

295

For the major storm condition simulated in Case 2, wave breaking-induced currents are more intensive compared to that in Case 1. In Fig. 13, we illustrate wave-induced current field superimposed on the vertical vorticity field, which is representative of energy dissipation due to wave breaking and bottom friction according to the vorticity conservation equation [e.g., *Chen et al.*, 1999]. The storm waves break on the ebb shoal, generating ap-

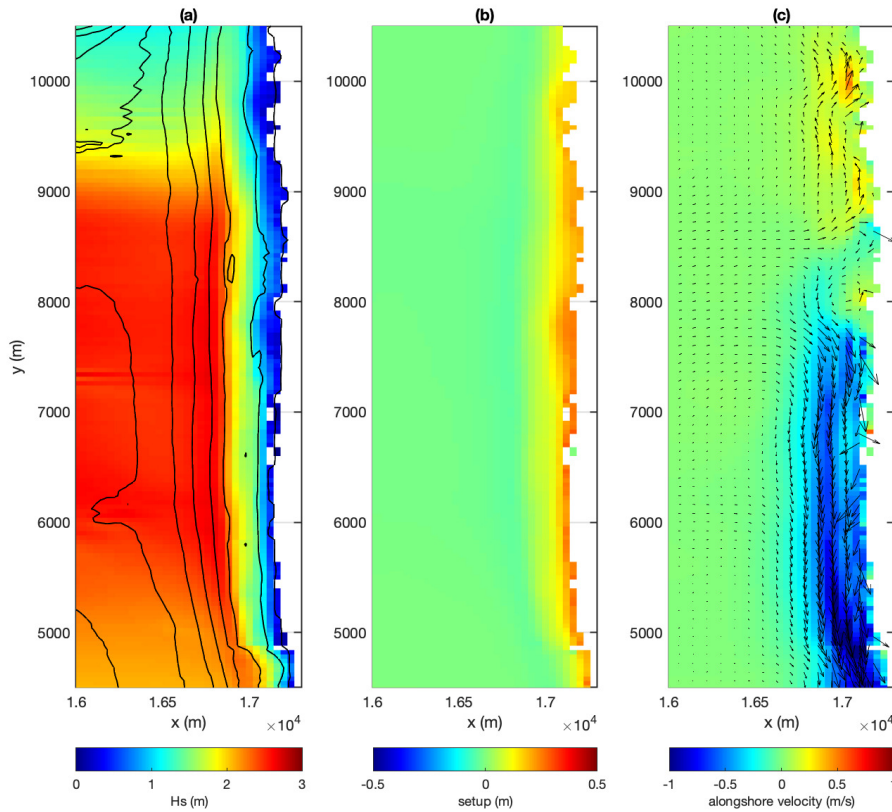


**Figure 14.** SWAN model result. Wave height distribution (a), wave setup (b), and wave-induced circulation (c, color represents alongshore velocity) in the nearshore region denoted in the dashed line block in Figure 11. Wave condition:  $H_{sig} = 2.49$  m,  $T_p = 11.1$  s, and  $\theta_p = 290^\circ$  measured at the CDIP 029 buoy.

296 parent vortices on the shoal, which are absent in Case 1. Wave breaking induced currents on  
 297 the shoal basically move in the same direction as the dominant wave direction, which can be  
 298 explained by the major forcing term,  $\mathbf{k}D_w$ , where  $\mathbf{k}$  is the wavenumber vector and  $D_w$  is en-  
 299 ergy dissipation, in the vortex form of wave force formulation [Smith, 2006; Shi et al., 2007].  
 300 In the nearshore region, the patterns of wave-induced current look similar to that in Case 1  
 301 but with a wider surfzone and larger current velocities caused by the overwhelming wave  
 302 breaking nearshore.

## 303 6.2 Comparison to the wave-averaged circulation model, NearCoM

304 The difference in the nearshore circulation induced by the wave fields with and with-  
 305 out the wave interference effect can be examined by the comparison between FUNWAVE and  
 306 NearCoM with the same offshore wave condition. Figure 14 shows the same plot as Figure  
 307 12 but from the NearCoM model for the wave condition in Case 1. As mentioned in the last  
 308 section, SWAN produced the wave focusing pattern (a), the same as in FUNWAVE, though  
 309 it cannot predict the small-scale fingering feature in the wave field. Responding to the wave  
 310 focusing pattern, the wave setup exhibits apparently nonuniform distribution in the along-  
 311 shore direction (b) with the higher setup around the wave focusing center ( $y \sim 7,000$  m). The

312 southward alongshore currents are generated by the obliquely incident waves in the south re-  
 313 gion ( $y < 8500$  m). The northward reversal flows appear in the north region ( $y > 8500$  m) as  
 314 a result of the pressure gradient forcing opposite to the wave forcing direction.

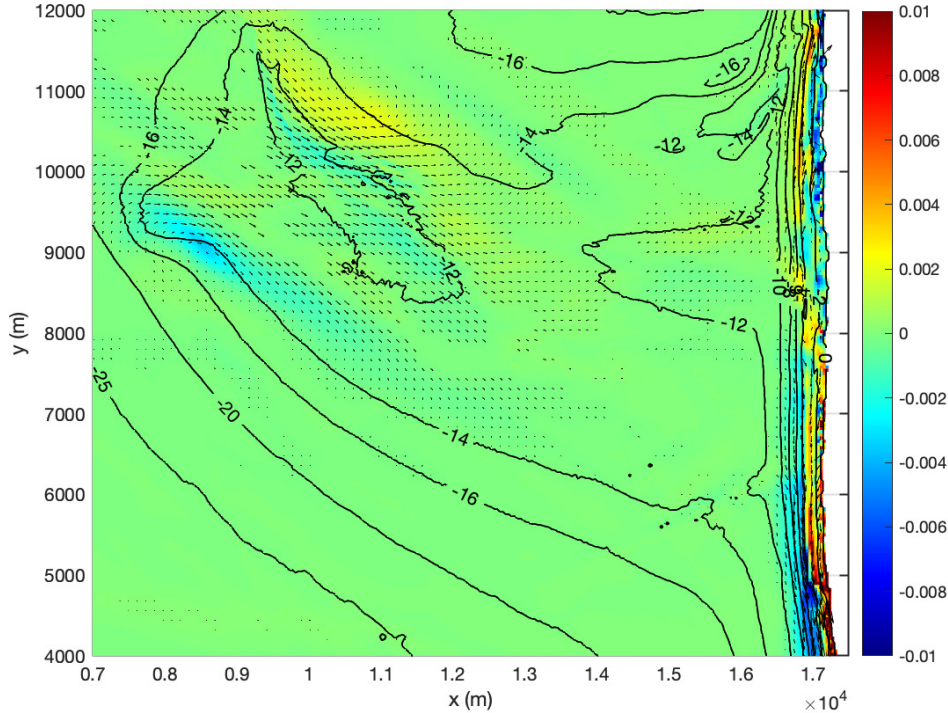


**Figure 15.** The same plot as Fig. 13 but from the NearCoM model. Case 2:  $H_{sig} = 5.1$  m,  $T_p = 14.29$  s, and  $\theta_p = 297^\circ$  measured at the CDIP 029 buoy.

315 For the storm scenario in Case 2, NearCoM predicted the offshore circulation on the  
 316 shoal and nearshore circulation as shown in Figure 15, similar to the results from FUN-  
 317 WAVE. In comparison to the FUNWAVE results (Figure 13), the wave-induced offshore cur-  
 318 rents produced by NearCoM are distributed more evenly on the shoal without the small-scale  
 319 strip features as shown in Figure 13. The vertical vorticity in FUNWAVE is more intense  
 320 nearshore, probably due to the averaging in a short time period.

321 In general, the NearCoM model predicted wave-averaged processes which are similar  
 322 to those predicted by FUNWAVE. However, the wave-induced circulation field predicted by  
 323 NearCoM does not show much alongshore variation or small-scale structures. In addition,  
 324 the wave-induced currents in NearCoM are less energetic than FUNWAVE, which will be  
 325 discussed in the next section.

### 326 6.3 Temporal variability of wave-induced processes

327 Surf zone dynamics associated with wave breaking and wave-induced processes in-  
 328 volve a wide range of temporal scales [Geiman *et al.*, 2011]. The time-domain Boussinesq  
 329 model can provide a temporal variability of wave-driven nearshore circulation under the ran-  
 330 dom wave forcing and wave-current interaction [Chen *et al.*, 2003]. The energetics of wave-  
 331 driven current and the associated vertical vorticity field can be obtained by time-averaging  
 332 of the instantaneous wave velocity field over a relatively short time period, such as 20's wave

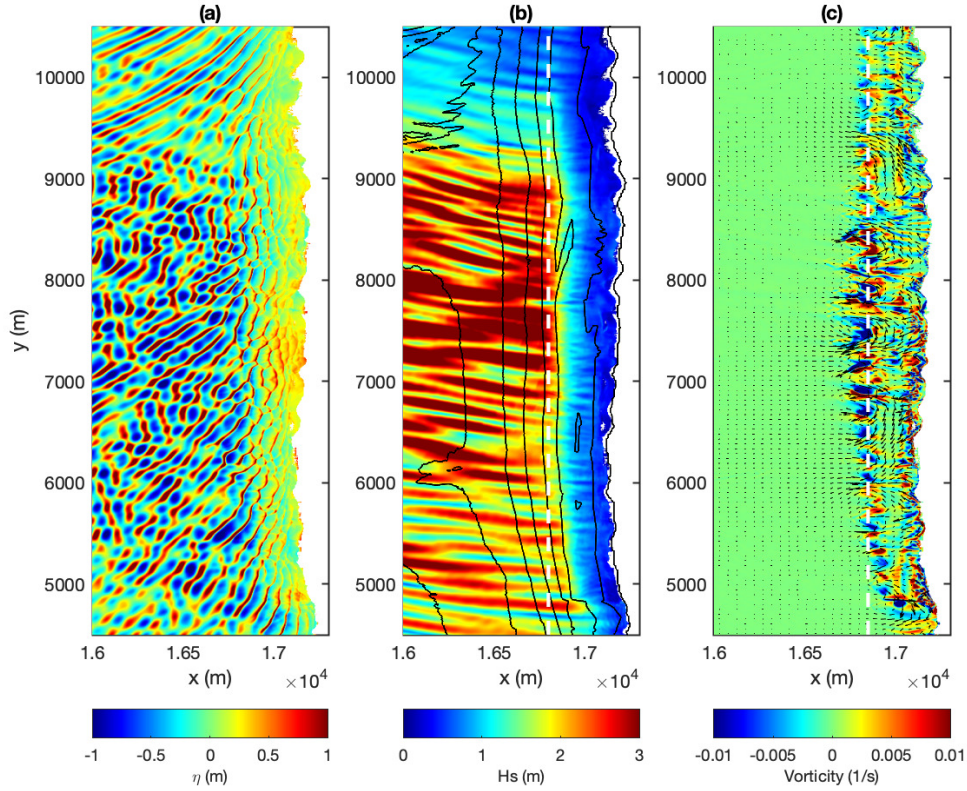


**Figure 16.** A snapshot of surface elevation (a), distributions of wave height (b) and vertical vorticity (c) in the nearshore region denoted in the dashed line block in Fig. 8. The wave-averaged quantities are processed in the time period of 1800 - 2040 s (20 peak periods). Case 1:  $H_{sig} = 2.49$  m,  $T_p = 11.1$  s, and  $\theta_p = 290^\circ$  measured at the CDIP 029 buoy. White dashed lines are transects used for the FFT processing.

333 peak periods as suggested by *Chen et al.* [2003]. The vertical vorticity is generated by indi-  
 334 vidual random breakers in the surfzone, producing shear waves different from those driven  
 335 by a wave-averaged circulation model [*Chen et al.*, 2003]. To examine the correlation be-  
 336 tween wave interference and wave-induced circulation field, we demonstrate the vortex injec-  
 337 tion in the early stage of vorticity generation before shear waves are fully developed.

338 Figure 16 shows the results analyzed in the time period of 1800 s - 2040 s (20 peak  
 339 periods). In the figure, a snapshot of surface elevation (a) is also presented to show wave in-  
 340 terference patterns. The distribution of wave height (b) looks similar to that in Figure 12 (a)  
 341 except the modulation patterns are more striking due to the shorter time processing versus  
 342 the longer time processing (1200 s). As mentioned earlier, the nodal lines caused by wave  
 343 interference are persistent and would not change much with time. Panel (c) shows the early  
 344 stage of vertical vorticity generation, revealing that the injection of vortex eddies closely co-  
 345 incides with the fingering patterns of the offshore wave field.

346 To confirm the correlation between the wave modulation and vorticity generation, we  
 347 applied Fast Fourier Transform (FFT) to both the alongshore distributions of wave height and  
 348 vertical vorticity along the transects denoted by the white dashed lines in Figure 16 (b) and  
 349 (c). Fig. 17 compares the amplitudes of FFT for wave height and vorticity modulations ver-

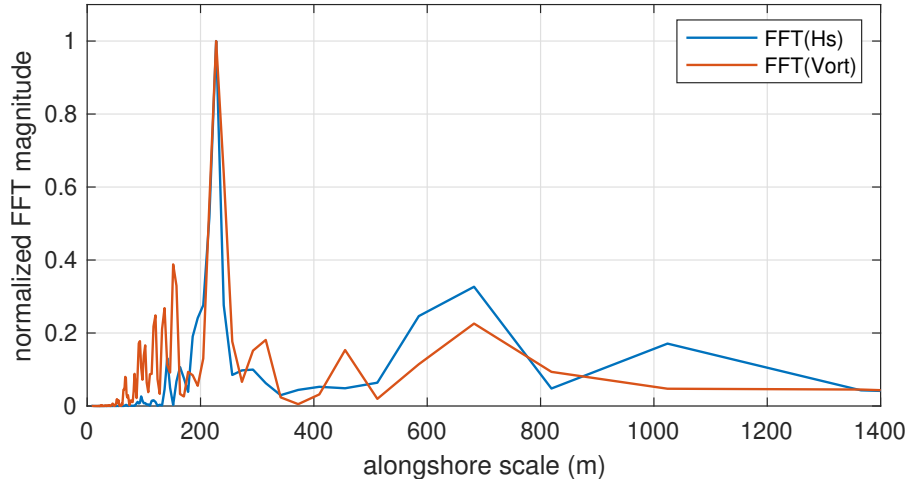


**Figure 17.** Amplitudes of the Fast Fourier Transform for alongshore wave modulation (blue) and vorticity modulation (red) along the transects denoted by the white dashed lines in Figure 16 (b) and (c). The amplitudes were normalized by the corresponding maximum FFT values.

350 sus alongshore scales. The amplitudes in the comparison were normalized by their maximum  
 351 values of FFT. For the wave height modulation (blue), the peak of the FFT amplitude ap-  
 352 pears at 220 m, meaning that the alongshore scale of the nodal lines is around 220 m. As  
 353 expected, the peak for the vorticity field (red) occurs around the same place, indicating the ma-  
 354 jor length scale for vortices in the early stage is consistent with the scale of the nodal lines.  
 355 The vorticity generation is closely correlated to the wave interference caused wave height  
 356 modulation.

357 The energetic and transport features of vertical vorticity can be found in the snapshots  
 358 of the vorticity field in Figure 18, which are taken 600 s apart, starting from  $t = 2040$  s. The  
 359 vertical vorticity in each snapshot was calculated by averaging over the same short time peri-  
 360 od (240 s) as the case above. The figure shows that the instantaneous vorticity is advected  
 361 by alongshore currents (refer to Figure 12) southward in the south region ( $y < 8000$  m) and  
 362 northward in the north region. Small-scale rip current cells appear all over the place inside  
 363 the surf zone.

## 364 7 Conclusions

365 The study was motivated by the finding in *Smit et al.* [2016] who observed the out-  
 366 standing wave interference phenomena at the ebb-tidal delta of San Francisco, CA. Our  
 367 curiosity is how the wave interference affects the nearshore wave field and wave-induced  
 368 nearshore circulation, which has been studied previously using wave-averaged circulation  
 369 models. In this study, we used the time-domain Boussinesq wave model, FUNWAVE-TVD,  
 370 to investigate waves and wave-induced circulation processes with emphasizing wave inter-  
 371 ference caused by the ebb shoal and its effects on nearshore circulation. The model results were  
 372 compared with the wave-averaged model, NearCoM, used in a previous study.

373 The Boussinesq model predicted the wave interference phenomena caused by the ebb  
 374 shoal, with interference scales of 150 ~ 310 m, consistent with the Radar observation by *Smit*  
 375 *et al.* [2016]. The model shows the small-scale fingering structures in the wave height dis-  
 376 tribution resulting from wave interference, which are persistent with nodal lines unchanged  
 377 with time. The wave height modulation can reach up to 50% of the wave height predicted by  
 378 the conventional phase-averaged wave model. The field observation offshore of Ocean Beach

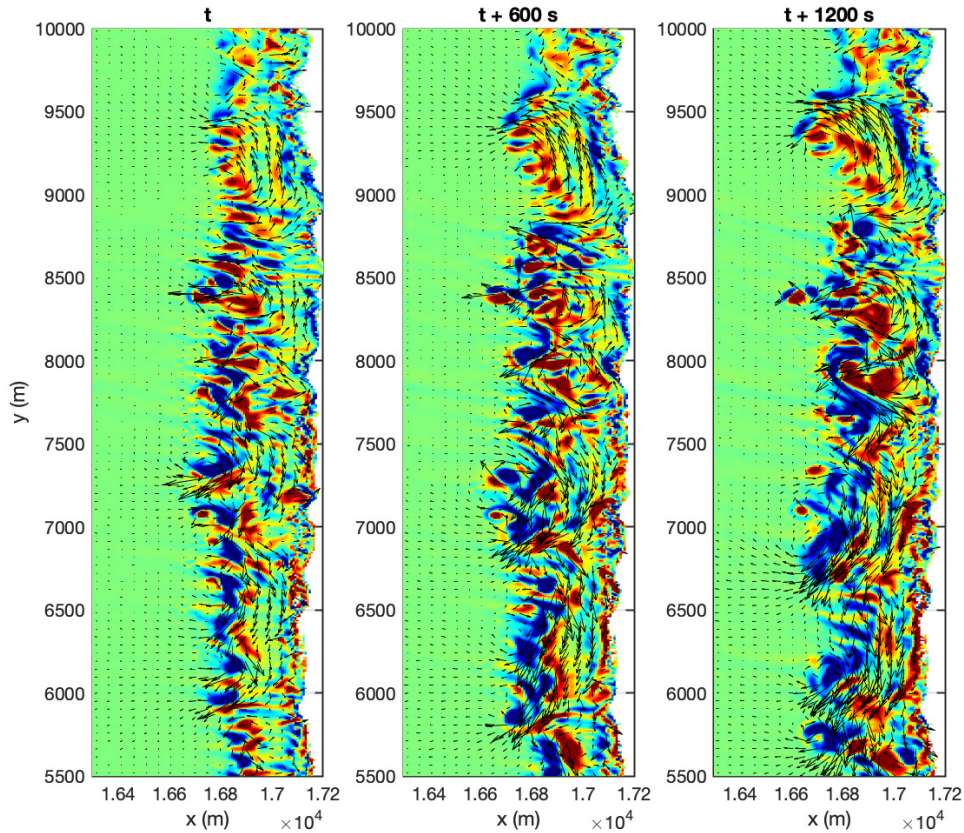


**Figure 18.** Time sequence of current and vorticity field averaged over 240 s. Case 1:  $H_{sig} = 2.49$  m,  $T_p = 11.1$  s, and  $\theta_p = 290^\circ$  measured at the CDIP 029 buoy.

379 in the previous studies did not resolve the wave field modulation due to the sparse deploy-  
 380 ments of instruments.

381 The impact of wave interference on nearshore circulation is significant. The modulated  
 382 wave field induces small-scale flow structures in nearshore circulation, which were not pre-  
 383 dicted by the conventional wave-averaged circulation model. However, the small-scale mod-  
 384 ulation in the wave field seems not to generate alongshore variation in wave setup in such  
 385 scales. Therefore, in a large-scale view, the alongshore currents predicted by the Boussinesq  
 386 model still keep the major features shown in the wave-averaged circulation model, such as  
 387 the flow divergence caused by the pressure gradient force associated with the wave setup. For  
 388 a storm wave condition, waves break on the ebb shoal, inducing shoreward-directed currents  
 389 in the breaking region, indicated in both the Boussinesq and the wave-averaged circulation  
 390 model. The Boussinesq model shows smaller-scale stripe features of breaking wave-induced  
 391 current and vorticity fields versus the wave-averaged circulation model in which the current  
 392 and vorticity are evenly distributed on the shoal.

393 The time-domain Boussinesq model predicted the temporal variability of wave-induced  
 394 processes. The wave field modulation is highly correlated to the vorticity generation nearshore.  
 395 The alongshore varying wave breakers tied with wave interference patterns are sources of the  
 396 vorticity generation and cause energetic vortex eddies in the surf zone.

397 The nearshore circulation at Ocean Beach is affected by tides and tidal currents, es-  
 398 pecially in the nearshore area close to the inlet as discussed in *Shi et al.* [2011] and *Hansen*  
 399 *et al.* [2013]. Due to a large computational cost, we did not include tides in the time-domain  
 400 Boussinesq model. However, the model reveals more complete physical processes associated  
 401 with wave interference effects and provides a promising prospect for the future research on  
 402 wave-induced processes in the large ebb shoal-beach system.

403 **Data Availability Statement** The post-processed numerical results and measurement data  
 404 used in this research are archived at (<http://doi.org/10.5281/zenodo.6336156>).

405 **Acknowledgements** The first author, Yu Zhang, would like to thank the Center for Applied  
 406 Coastal Research at the University of Delaware for hosting her study visit. Fengyan Shi  
 407 was supported by the College of Engineering, University of Delaware, during his sabbatical  
 408 leave. This research was supported in part through the use of Information Technologies  
 409 (IT) resources at the University of Delaware. The package of FUNWAVE-TVD, including  
 410 source codes, benchmark tests, examples for various model applications is maintained at the  
 411 GITHUB site: <https://github.com/fengyanshi/FUNWAVE-TVD>.

## 412 References

- 413 Akrish, G., P. Smit, M. Zijlema, and A. Reniers (2020), Modelling statistical wave  
 414 interferences over shear currents, *Journal of Fluid Mechanics*, 891, A2, doi:  
 415 10.1017/jfm.2020.143.
- 416 Barnard, P. L., J. E. Hansen, and L. H. Erikson (2012), Synthesis study of an erosion  
 417 hot spot, ocean beach, california, *Journal of Coastal Research*, 28(4), 903–922, doi:  
 418 10.2112/JCOASTRES-D-11-00212.1.
- 419 Booij, N., R. C. Ris, and L. H. Holthuijsen (1999), A third-generation wave model for coastal  
 420 regions: 1. Model description and validation, *Journal of Geophysical Research: Oceans*,  
 421 104(C4), 7649–7666, doi:10.1029/98JC02622.
- 422 Brown, J., J. MacMahan, A. Reniers, and E. Thornton (2009), Surf zone diffusivity on a rip-  
 423 channeled beach, *Journal of Geophysical Research: Oceans*, 114(C11).
- 424 Chakrabarti, A., S. R. Brandt, Q. Chen, and F. Shi (2017), Boussinesq modeling of wave-  
 425 induced hydrodynamics in coastal wetlands, *Journal of Geophysical Research: Oceans*,  
 426 122(5), 3861–3883.
- 427 Chawla, A., H. T. Özkan Haller, and J. T. Kirby (1998), Spectral model for wave transfor-  
 428 mation and breaking over irregular bathymetry, *Journal of Waterway, Port, Coastal and*  
 429 *Ocean Engineering*, 124(4), 189–198.
- 430 Chen, J.-L., F. Shi, T.-J. Hsu, and J. T. Kirby (2014), NearCoM-TVD—A quasi-3D nearshore  
 431 circulation and sediment transport model, *Coastal Engineering*, 91, 200–212, doi:  
 432 10.1016/j.coastaleng.2014.06.002.
- 433 Chen, Q. (2006), Fully nonlinear Boussinesq-type equations for waves and cur-  
 434 rents over porous beds, *Journal of Engineering Mechanics*, 132(2), 220–230, doi:  
 435 10.1061/(ASCE)0733-9399(2006)1232:2(220).
- 436 Chen, Q., R. A. Dalrymple, J. T. Kirby, A. B. Kennedy, and M. C. Haller (1999), Boussinesq  
 437 modeling of a rip current system, *Journal of Geophysical Research: Oceans*, 104(C9),  
 438 20,617–20,637, doi:10.1029/1999JC900154.
- 439 Chen, Q., J. T. Kirby, R. A. Dalrymple, A. B. Kennedy, and A. Chawla (2000), Boussinesq  
 440 modeling of wave transformation, breaking and runup. II: 2D, *Journal of Waterway, Port,*  
 441 *Coastal and Ocean Engineering*, 126(1), 48–56.
- 442 Chen, Q., J. T. Kirby, R. A. Dalrymple, F. Shi, and E. B. Thornton (2003), Boussinesq mod-  
 443 eling of longshore currents, *Journal of Geophysical Research: Oceans*, 108(C11), 3362,  
 444 doi:10.1029/2002JC001308.

- 445 Dalrymple, R. A. (1975), A mechanism for rip current generation on an open coast, *Journal*  
 446 *of Geophysical Research*, 80(24), 3485–3487, doi:10.1029/JC080i024p03485.
- 447 Dalrymple, R. A., J. H. MacMahan, A. J. Reniers, and V. Nelko (2011), Rip currents, *Annual*  
 448 *Review of Fluid Mechanics*, 43, 551–581, doi:10.1146/annurev-fluid-122109-160733.
- 449 Eshleman, J. L., P. L. Barnard, L. H. Erikson, and D. M. Hanes (2007), Coupling alongshore  
 450 variations in wave energy to beach morphologic change using the SWAN wave model at  
 451 Ocean Beach, San Francisco, CA, in *10th International Workshop on Wave Hindcasting*  
 452 *and Forecasting (Oahu, Hawaii)*, Paper F, vol. 4, p. 20p, Citeseer.
- 453 Fregoso, T. A., R.-F. Wang, E. Ateljevich, and B. E. Jaffe (2017), A new seamless, high-  
 454 resolution digital elevation model of the san francisco bay-delta estuary, california, *Tech.*  
 455 *rep.*, US Geological Survey.
- 456 Geiman, J. D., J. T. Kirby, A. J. H. M. Reniers, and J. H. MacMahan (2011), Effects of wave  
 457 averaging on estimates of fluid mixing in the surf zone, *Journal of Geophysical Research:*  
 458 *Oceans*, 116, C04,006, doi:10.1029/2010JC006678.
- 459 Hansen, J. E., E. Elias, J. H. List, L. H. Erikson, and P. L. Barnard (2013), Tidally influenced  
 460 alongshore circulation at an inlet-adjacent shoreline, *Continental Shelf Research*, 56, 26–  
 461 38, doi:10.1016/j.csr.2013.01.017.
- 462 Hansen, J. E., T. T. Janssen, B. Raubenheimer, F. Shi, P. L. Barnard, and I. S. Jones (2014),  
 463 Observations of surfzone alongshore pressure gradients onshore of an ebb-tidal delta,  
 464 *Coastal Engineering*, 91, 251–260, doi:10.1016/j.coastaleng.2014.05.010.
- 465 Johnson, D. (2004), Transient rip currents and nearshore circulation on a swell-dominated  
 466 beach, *Journal of Geophysical Research*, 109, C02,026, doi:10.1029/2003JC001798.
- 467 Kennedy, A. B., Q. Chen, J. T. Kirby, and R. A. Dalrymple (2000), Boussinesq modeling of  
 468 wave transformation, breaking and runup. I: 1D, *Journal of Waterway, Port, Coastal and*  
 469 *Ocean Engineering*, 126(1), 39–47.
- 470 Kennedy, A. B., J. T. Kirby, Q. Chen, and R. A. Dalrymple (2001), Boussinesq-type  
 471 equations with improved nonlinear performance, *Wave Motion*, 33, 225–243, doi:  
 472 10.1016/S0165-2125(00)00071-8.
- 473 Kirby, J. T. (2016), Boussinesq models and their application to coastal processes across a  
 474 wide range of scales, *Journal of Waterway, Port, Coastal, and Ocean Engineering*, 142(6),  
 475 03116,005, doi:10.1061/(ASCE)WW.1943-5460.0000350.
- 476 Komen, G. J., L. Cavaleri, M. Donelan, K. Hasselmann, S. Hasselmann, and P. Janssen  
 477 (1996), *Dynamics and modelling of ocean waves*.
- 478 Lam, M. Y., M. Malej, F. Shi, and K. Ghosh (2018), Profiling and optimization of  
 479 FUNWAVE-TVD on high performance computing (HPC) machines, *Tech. rep.*, Army En-  
 480 gineer Waterways Experiment Station, Vicksburg, MS.
- 481 Lesser, G. R., J. A. Roelvink, J. T. M. van Kester, and G. S. Stelling (2004), Development  
 482 and validation of a three-dimensional morphological model, *Coastal Engineering*, 51(8-9),  
 483 883–915, doi:10.1016/j.coastaleng.2004.07.014.
- 484 Ma, G., F. Shi, and J. T. Kirby (2012), Shock-capturing non-hydrostatic model for  
 485 fully dispersive surface wave processes, *Ocean Modelling*, 43–44, 22–35, doi:  
 486 10.1016/j.ocemod.2011.12.002.
- 487 MacMahan, J., J. Brown, J. Brown, E. Thornton, A. Reniers, T. Stanton, M. Henriquez,  
 488 E. Gallagher, J. Morrison, M. J. Austin, et al. (2010), Mean lagrangian flow behavior on  
 489 an open coast rip-channeled beach: A new perspective, *Marine Geology*, 268(1-4), 1–15.
- 490 Mulligan, R. P., A. E. Hay, and A. J. Bowen (2010), A wave-driven jet over a rocky shoal,  
 491 *Journal of Geophysical Research*, 115(C10038), doi:10.1029/2009JC006027.
- 492 O’Reilly, W. C., C. B. Olfe, J. Thomas, R. Seymour, and R. Guza (2016), The california  
 493 coastal wave monitoring and prediction system, *Coastal Engineering*, 116, 118–132.
- 494 Salatin, R., Q. Chen, A. S. Bak, F. Shi, and S. R. Brandt (2021), Effects of wave coherence  
 495 on longshore variability of nearshore wave processes, *Journal of Geophysical Research:*  
 496 *Oceans*, 126, e2021JC017,641, doi:10.1029/2021JC017641.
- 497 Shi, F., J. Kirby, P. Newberger, and K. Haas (2005), Nearcom master program. version  
 498 2005.4: User’s manual and module integration, *Res. Rep*, 10.

- 499 Shi, F., J. T. Kirby, and K. Haas (2007), Quasi-3d nearshore circulation equations: a cl-  
500 vortex force formulation, in *Coastal Engineering 2006: (In 5 Volumes)*, pp. 1028–1039,  
501 World Scientific.
- 502 Shi, F., D. M. Hanes, J. T. Kirby, L. Erikson, P. Barnard, and J. Eshleman (2011), Pressure-  
503 gradient-driven nearshore circulation on a beach influenced by a large inlet-tidal shoal  
504 system, *Journal of Geophysical Research*, *116*, C04,020, doi:10.1029/2010JC006788.
- 505 Shi, F., J. T. Kirby, J. C. Harris, J. D. Geiman, and S. T. Grilli (2012), A high-order adaptive  
506 time-stepping TVD solver for Boussinesq modeling of breaking waves and coastal inunda-  
507 tion, *Ocean Modelling*, *43*, 36–51, doi:10.1016/j.ocemod.2011.12.004.
- 508 Smit, P. B., and T. T. Janssen (2013), The evolution of inhomogeneous wave statistics  
509 through a variable medium, *Journal of Physical Oceanography*, *43*(8), 1741–1758, doi:  
510 10.1175/JPO-D-13-046.1.
- 511 Smit, P. B., T. T. Janssen, and T. H. C. Herbers (2015), Stochastic modeling of inhomoge-  
512 neous ocean waves, *Ocean Modelling*, *96*, 26–35, doi:10.1016/j.ocemod.2015.06.009.
- 513 Smit, P. B., R. Bland, T. T. Janssen, and B. Laughlin (2016), Remote sensing of nearshore  
514 wave interference, *Journal of Geophysical Research: Oceans*, *121*, 3409–3421, doi:  
515 10.1002/2016JC011705.
- 516 Smith, J. A. (2006), Wave-current interactions in finite depth, *Journal of Physical Oceanog-*  
517 *raphy*, *36*, 1403–1419.
- 518 Spydell, M., and F. Feddersen (2009), Lagrangian drifter dispersion in the surf zone: Di-  
519 rectionally spread, normally incident waves, *Journal of Physical Oceanography*, *39*(4),  
520 809–830.
- 521 Tolman, H. L. (1991), A third-generation model for wind waves on slowly varying, unsteady,  
522 and inhomogeneous depths and currents, *Journal of Physical Oceanography*, *21*(6), 782–  
523 797.
- 524 Vincent, C. L., and M. J. Briggs (1989), Refraction–diffraction of irregular waves over a  
525 mound, *Journal of Waterway, Port, Coastal, and Ocean Engineering*, *115*(2), 269–284.
- 526 Wei, G., J. T. Kirby, S. T. Grilli, and R. Subramanya (1995), A fully nonlinear Boussinesq  
527 model for surface waves. Part 1. Highly nonlinear unsteady waves, *Journal of Fluid Me-*  
528 *chanics*, *294*, 71–92, doi:10.1017/S0022112095002813.
- 529 Yuan, Y., F. Shi, J. Kirby, and F. Yu (2020), Multiple-gpu acceleration of the boussinesq-type  
530 wave model funwave-tvd, *J. Adv. Model. Earth Syst*, *12*(5), 1–19.
- 531 Zijlema, M., G. Stelling, and P. Smit (2011), Swash: An operational public domain code for  
532 simulating wave fields and rapidly varied flows in coastal waters, *Coastal Engineering*,  
533 *58*(10), 992–1012.